

---

# MAMBA-X-NET: DUAL-INPUT MAMBA-ENHANCED CROSS-ATTENTION NETWORK FOR LONGITUDINAL MRI SEGMENTATION

---

**Yovin Yahathugoda<sup>1</sup>, Davide Prezzi<sup>1,2</sup>, Piyalitt Ittichaiwong<sup>1</sup>, Vicky Goh<sup>1,2</sup>, Sébastien Ourselin<sup>1</sup>, and Michela Antonelli<sup>1</sup>**

<sup>1</sup>School of Biomedical Engineering & Imaging Sciences, King's College London, United Kingdom

<sup>2</sup>Department of Radiology, Guy's and St Thomas' NHS Foundation Trust, United Kingdom

December 1, 2025

## ABSTRACT

Active Surveillance (AS) is a treatment option for managing low and intermediate-risk prostate cancer (PCa), aiming to avoid overtreatment while monitoring disease progression through serial MRI and clinical follow-up. Accurate prostate segmentation is an important preliminary step for automating this process, enabling automated detection and diagnosis of PCa. However, existing deep-learning segmentation models are often trained on single-time-point and expertly annotated datasets, making them unsuitable for longitudinal AS analysis, where multiple time points and a scarcity of expert labels hinder their effective fine-tuning. To address these challenges, we propose MambaX-Net, a novel semi-supervised, dual-scan 3D segmentation architecture that computes the segmentation for time point  $t$  by leveraging the MRI and the corresponding segmentation mask from the previous time point. We introduce two new components: (i) a Mamba-enhanced Cross-Attention Module, which integrates the Mamba block into cross attention to efficiently capture temporal evolution and long-range spatial dependencies, and (ii) a Shape Extractor Module that encodes the previous segmentation mask into a latent anatomical representation for refined zone delination. Moreover, we introduce a semi-supervised self-training strategy that leverages pseudo-labels generated from a pre-trained nnU-Net, enabling effective learning without expert annotations. MambaX-Net was evaluated on a longitudinal AS dataset, and results showed that it significantly outperforms state-of-the-art U-Net and Transformer-based models, achieving superior prostate zone segmentation even when trained on limited and noisy data.

**Keywords** Active Surveillance · Deep Learning · Prostate Cancer · Prostate MRI · Segmentation

## 1 Introduction

Prostate cancer (PCa) is one of the most prevalent cancers among men in Western countries [1]. The majority of patients diagnosed with PCa present with low-intermediate-risk disease (International Society of Urological Pathology, ISUP grade 1 and 2), localised to the prostate [2]. Active surveillance (AS) is a treatment option for low-intermediate-risk PCa, which limits unnecessary treatments and their adverse effects [3] while monitoring disease progression. Current AS protocols require regular clinical examinations, serum prostate-specific antigen (PSA) testing, repeated Magnetic Resonance Imaging (MRI) and biopsy to confirm progression [2]. Although MRI has emerged as an important non-invasive tool for selecting and monitoring patients in AS [4], its interpretation requires substantial expertise and remains time-intensive, particularly for complex AS cases [5], making Artificial Intelligence (AI) a promising approach to automate and streamline prostate MRI analysis, improving diagnostic efficiency [6].

---

Corresponding author: yovin.yahathugoda@kcl.ac.uk

A critical pre-requisite for AI-driven prostate MRI analysis is accurate segmentation of the whole prostate (WP) as well as its sub-regions, particularly the peripheral (PZ) and transition (TZ) zones, with the different zones having distinct pathogenetic features of PCa [7]. Accurate WP segmentation is essential for estimating prostate volume, a key requirement for calculating PSA density (PSAd), which helps distinguish elevated PSA caused by PCa from benign prostatic hyperplasia [5], while PZ and TZ segmentations are crucial priors for automated lesion detection[8].

Prostate zone segmentation approaches typically are based on either Convolutional Neural Networks (CNNs) or Transformers. While the CNN-based nnU-Net [9] remains state-of-the-art (SOTA) and a powerful baseline [10, 11], Transformer-based models such as SwinUNETR [12] are increasingly explored for their ability to capture long-range global context. Yet, Transformers often struggle to preserve fine-grained details and typically require large training datasets to surpass CNNs [13]. Yan et al. [13] reported that their hybrid CNN-ViT model, CCT-UNet, outperformed U-Net and SwinUNETR, though its Transformer backbone relied on a large training dataset. Huang et al. [14] showed that the U-Net was superior to a ViT in learning effectively from a small labelled dataset under semi-supervised settings. The findings suggest that while attention mechanisms may enhance CNNs, simple integration is insufficient; for example, a Global–Local Channel and Spatial Attention-enhanced U-Net [15] was outperformed by our standard nnU-Net baseline on the ProstateX dataset, suggesting that more advanced approaches are required to improve upon highly-optimised architectures.

These results underscore the need for novel architectures that can overcome the limitations of both CNNs and Transformers. Recently, the Mamba architecture [16] has gained popularity in medical imaging. Unlike Transformers that rely on a computationally intensive self-attention mechanism scaling quadratically with sequence length, Mamba scales linearly, offering significant advantages over Transformers, especially for 3D modalities like MRI. At its core, Mamba blocks use a selection mechanism that makes its parameters input-dependent to allow content-based reasoning. This allows the model to dynamically decide which information to keep and which to forget, effectively compressing relevant context into a fixed-size state and capturing long-range spatial dependencies. The selection mechanism in Mamba is enhanced by a hardware-aware algorithm that uses the parallel scan to run the recurrent computation in parallel on GPUs, combining the efficiency of recurrent models with the content-aware reasoning of Transformers. Recent works have integrated Mamba into hybrid architectures, including SegMamba [17], MUNet [18], and MambaBTS [19], which combine the powerful local feature extraction of CNNs with Mamba’s efficient global context modelling, leading to superior performance in medical image segmentation.

While Mamba-based architectures have achieved competitive performance in 3D segmentation tasks, they, like other SOTA prostate segmentation models, are exclusively designed for single-timepoint data [20], and have not been extended to longitudinal analysis, which is crucial in the context of AS. Single-timepoint models are inherently limited for longitudinal monitoring as they treat each scan in isolation, failing to leverage the rich temporal information available across patients’ imaging history and to capture the underlying anatomical changes. In other domains, such as brain imaging, SOTA longitudinal segmentation approaches typically rely on registering scans across different time points [21, 22]. However, these methods are often unreliable, as they are prone to registration errors, especially for prostate segmentation, where substantial non-rigid deformation over time makes registration challenging. In our prior work, we introduced the Dual-Scan Model (DSM) [23], which was the first attempt to incorporate longitudinal information for prostate MRI segmentation by jointly processing two subsequent time points. However, DSM relied on pure cross-attention combined with SimAM blocks [24], which is effective for local spatial suppression but cannot effectively capture long-range dependencies, and often produces irregular segmentations at the prostate apex.

In addition to architectural design, model performance also depends on the availability of expertly annotated datasets, which are particularly limited in AS due to the time-consuming task of labelling multiple time-points per patient [25, 26]. Pre-training on public datasets followed by fine-tuning on the target domain dataset is a promising strategy [27, 28, 29], but fine-tuning on the target domain dataset is still dependent on the availability of expert annotations, which can be scarce for longitudinal datasets.

To address both the lack of longitudinal modelling and the scarcity of expert-annotated longitudinal data, we introduce MambaX-Net, a novel 3D segmentation model designed specifically for longitudinal data, together with a self-training framework that leverages pseudo-labels to reduce annotation requirements. MambaX-Net is a dual-scan architecture that extends a 3D nnU-Net to segment the image at time point  $t$  using information from the image and the corresponding segmentation mask at time point  $t - 1$ . Its novelty lies in two key aspects: (i) the Mamba-enhanced Cross-Attention Module (M-CAM), which integrates Mamba blocks into cross-attention [30] to capture temporal dependencies, and (ii) the injection of the segmentation mask from the previous time point through the Shape Extractor Module (SEM), a sequential block of convolutional layers with ReLU activations that encodes the prostate zone mask into a latent representation of key anatomical features. Within the proposed self-training framework, pseudo-labels for all the AS timepoints are generated using an nnU-Net model trained on a public dataset. The pseudo-label at  $t - 1$  is provided to

MambaX-Net during both training and inference for segmentation refinement, whereas the pseudo-label at  $t$  is used only for loss calculation during fine-tuning.

We evaluated MambaX-Net against three SOTA baselines (nnU-Net-V2, SwinUNETR-V2, SegMamba) as well as the DSM. Experimental results show that MambaX-Net significantly outperforms all four models, generating more accurate prostate zone segmentations even when trained on a reduced dataset with noisy labels. This performance gain derives from MambaX-Net’s ability to capture global anatomical relationships through M-CAM and refine segmentation boundaries with SEM, resulting in more accurate and robust prostate zone segmentation, particularly in data-limited settings.

## 2 Methods

This section presents the architecture of our novel MambaX-Net model, its core components, and the loss function used to train the model.

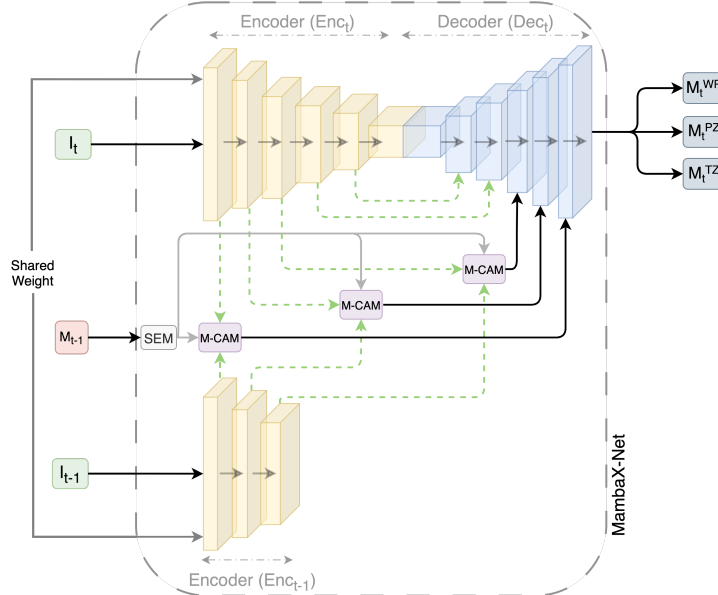


Figure 1: High-level architecture of MambaX-Net showing a U-Net-like dual-encoder structure ( $Enc_t$ ,  $Enc_{t-1}$ ) with shared weights for processing scans at two time points ( $I_t$  and  $I_{t-1}$ ), and a single decoder ( $Dec_t$ ). The M-CAM block fuses latent features from  $I_t$  and  $I_{t-1}$  with the SEM output, producing enhanced representations for prostate zone segmentation.

### 2.1 MambaX-Net Architecture Overview

The MambaX-Net architecture shown in Figure 1 extends the 3D nnU-Net encoder-decoder architecture, originally designed for single-timepoint data, with key architectural improvements that enable the integration of longitudinal information of the same patient from two sequential MRI scans (time point  $t$  and  $t - 1$ ) and the prior segmentation mask (time point  $t - 1$ ).

For each patient, let  $I_t$  denote the image to be segmented at time point  $t$ ,  $I_{t-1}$  the image acquired at time point  $t - 1$ , and  $M_{t-1}$  its corresponding 3-channel pseudo-label representing the whole prostate (WP), peripheral zone (PZ), and transition zone (TZ). MambaX-Net employs dual encoders,  $Enc_t$  and  $Enc_{t-1}$ , with shared weights to process  $I_t$  and  $I_{t-1}$ , respectively, together with a decoder,  $Dec_t$ , analogous to a standard U-Net architecture.  $Enc_t$  consists of six downsampling blocks to extract multi-scale feature maps ( $f_t^i, i \in \{1, \dots, 6\}$ ) from  $I_t$ , while the auxiliary encoder  $Enc_{t-1}$  is truncated to extract only the top three feature maps ( $f_{t-1}^i, i \in \{1, \dots, 3\}$ ) from  $I_{t-1}$ . This design choice was determined empirically during hyperparameter optimisation. Limiting  $Enc_{t-1}$  to these feature levels reduces computational complexity while preserving an optimal trade-off between high-resolution spatial details from shallower layers and rich semantic context from deeper layers.

In parallel, the Shape Extraction Module (SEM) shown in Figure 1, that comprises three sequential blocks (3D convolution layer followed by a ReLU activation layer), encodes  $M_{t-1}$  into a latent representation  $f_t^{SEM}$  capturing key

anatomical features, such as the size and shape of the prostate. M-CAM then takes as input  $f_t^i$ , and  $f_{t-1}^i$  combined with  $f_{t-1}^{SEM}$  to perform implicit image registration in the feature space across  $I_t$ ,  $I_{t-1}$ , and  $M_{t-1}$ , and integrate longitudinal information into a latent representation.

The fused features from M-CAM are injected into the last three upsampling blocks of the decoder, whereas the earlier blocks rely solely on standard skip connections. The model outputs a three-channel 3D segmentation mask ( $M_t$ ) comprising WP, PZ, and TZ.

## 2.2 SEM and M-CAM for Latent Feature Fusion

The proposed Mamba-enhanced Cross-Attention Module (M-CAM), shown in Figure 2, leverages Mamba blocks [16] to efficiently model long-range dependencies with linear scaling, providing robust performance across training datasets of varying sizes. M-CAM is the core architectural component of MambaX-Net, designed to align and fuse feature maps  $f_t^i$ ,  $f_{t-1}^i$  and  $f_{t-1}^{SEM}$ .

First,  $f_t^i$  and  $f_{t-1}^i$  are processed by a patch embedding layer, consisting of a linear layer and a rearrangement operation, followed by a normalisation layer. This yields the 3D patch embeddings  $P_t$  and  $P_{t-1} \in \mathbb{R}^{B \times N \times E}$ , where  $B$  is the batch size,  $N$  is the number of patches, and  $E$  is the embedding dimension.

Because the dimensionality of  $f_{t-1}^{SEM} (\mathbb{R}^{B \times C \times D \times H \times W})$ , where  $C = 3$  denotes the number of channels and  $D$ ,  $H$ , and  $W$  represent depth, height, and width), differs from that of  $P_{t-1}$ , both must be reshaped to align their dimensions before fusion. To this aim,  $f_{t-1}^{SEM}$  is reshaped to  $(B \times 3D \times H \times W)$ , while  $P_{t-1}$  is expanded to  $(B \times 1 \times N \times E)$ . The aligned tensors are then fused by element-wise addition with broadcasting, producing  $P_{fused,t-1}$ , which is passed through a ReLU activation to reintroduce non-linearity, followed by a 2D convolution to restore the embedding shape  $(B \times N \times E)$ .

Both patch embeddings,  $P_t$  and  $P_{fused,t-1}$ , are processed by Mamba blocks to capture long-range dependencies. A cross-attention layer then aligns the two Mamba-enhanced feature maps to generate a single fused representation. The output of the cross-attention layer is passed through an Unpack Embedding block, which converts the patch sequence back into a spatial feature map,  $f_{att}^i$ . Using a residual connection,  $f_{att}^i$  is combined with the original input feature map  $f_t^i$  via element-wise addition followed by a ReLU activation to produce the M-CAM’s final output,  $f_{CAM}^i$ . Element-wise addition preserves the feature map’s dimensions, avoiding the extra downsampling required by concatenation.

A key design choice in integrating SEM with M-CAM is to inject  $f_{t-1}^{SEM}$  after the patch embedding layer rather than before. The patch embedding layer projects semantically rich feature maps into a sequence of patches, effectively translating the spatial grid into a format suitable for Mamba and cross-attention. Injecting  $f_{t-1}^{SEM}$  before the patch embedding layer would create patches from a composite feature map, where the semantic content of  $f_{t-1}^i$  could be distorted by structural details from  $f_{t-1}^{SEM}$ , leading to less distinct and meaningful representations. By contrast, adding  $f_{t-1}^{SEM}$  after the patch embedding layer allows structural information to refine and guide the semantic representations in  $P_{t-1}$ , without disrupting their encoding. This design also makes M-CAM modular: if a prior segmentation mask is unavailable, the SEM branch (including ReLU and Conv2D layers) can simply be omitted. However, removing  $f_{t-1}^{SEM}$  eliminates its semantic enhancement and negatively impacts the overall model performance.

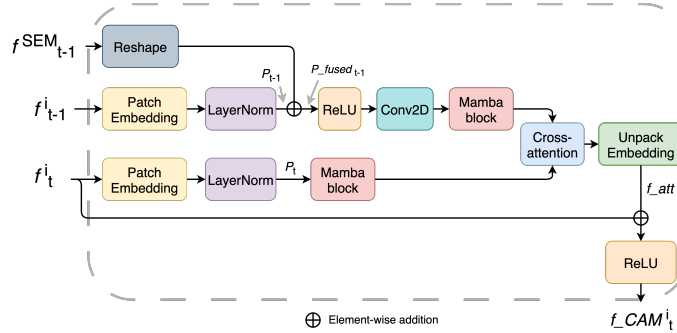


Figure 2: The Mamba-enhanced Cross-Attention Module (M-CAM) structure.

### 2.3 Loss Function

Designing an effective loss function is crucial for accurate prostate segmentation, particularly at the apex and base, where the gland is small and anatomically irregular. Previous research has shown that dice-cross-entropy (DiceCE) loss struggles with segmenting irregular regions, while the use of the Focal and Tversky loss functions enables the loss to focus on hard negative examples, thereby reducing false positives and false negatives [11]. For this reason, we employed a modified version of the Focal Tversky Dice Cross-Entropy loss (FT\_DCE), shown in equation (1), where instead of averaging the three loss components (Focal, Dice, and Tversky), we combined the Focal and Tversky losses (FT) following [31], and incorporated them with the DiceCE loss [9] using a weighted sum, with the weight parameter  $\omega$  set empirically through hyperparameter optimisation.

$$\mathcal{L}_{(\text{FT\_DCE})} = \omega \mathcal{L}_{\text{DiceCE}} + (1 - \omega) \mathcal{L}_{\text{FT}} \quad (1)$$

$\mathcal{L}_{\text{DiceCE}}$  is expressed in equation (2) with  $\mathcal{L}_{\text{Dice}}$  and  $\mathcal{L}_{\text{BCE}}$  defined by equations (3) and (4), respectively.

$$\mathcal{L}_{\text{DiceCE}} = \mathcal{L}_{\text{Dice}} + \mathcal{L}_{\text{BCE}} \quad (2)$$

$$\mathcal{L}_{\text{Dice}} = 1 - \frac{2 \sum_{i=1}^N p_i g_i}{\sum_{i=1}^N p_i^2 + \sum_{i=1}^N g_i^2} \quad (3)$$

$$\mathcal{L}_{\text{BCE}} = \begin{cases} -\log(p_i) & \text{if the true label } g_i \text{ is 1} \\ -\log(1 - p_i) & \text{if the true label } g_i \text{ is 0} \end{cases} \quad (4)$$

where for each voxel  $i$ ,  $p_i \in [0, 1]$  is the predicted probability and  $g_i \in \{0, 1\}$  the ground-truth. In addition to  $\mathcal{L}_{\text{DiceCE}}$ , the total loss FT\_DCE includes also  $\mathcal{L}_{\text{FT}}$ , which is defined by equation (5)

$$\mathcal{L}_{\text{FT}} = (1 - T(\alpha, \beta))^{1/\gamma} \quad (5)$$

with,  $T(\alpha, \beta)$  expressed by equation (6) and  $\gamma$  set empirically.

$$T(\alpha, \beta) = \frac{\sum_{i=1}^N p_i g_i}{\sum_{i=1}^N p_i g_i + \alpha \sum_{i=1}^N p_i g_i + \beta \sum_{i=1}^N p_i g_i} \quad (6)$$

where  $\alpha$  and  $\beta$  control the penalisation effect for false-positives (FPs) and false-negatives (FNs), respectively and are set empirically through hyperparameter optimisation.

## 3 Experiments

MambaX-Net was compared with three single-time-point SOTA baseline models (nnU-Net-V2, SwinUNETR-V2, SegMamba) as well as our previous dual-scan model (DSM). Performance was measured using the Dice Similarity Coefficient (DSC) and the 95th percentile Hausdorff Distance (HD95), expressed in millimetres (mm).

### 3.1 Datasets

Experiments were performed on two datasets: the publicly available PI-CAI dataset [32], and the in-house (private) AS dataset, which was collected at Guy's and St Thomas' Hospital with the necessary consent and ethics approval for analysis granted by the Guy's Cancer Cohort ethics committee (REC 23/NW/0105). PI-CAI was utilised for pre-training and validation of the MambaX-Net backbone, while the AS dataset was employed for model fine-tuning and testing.

The PI-CAI dataset consists of 1376 bpMRI acquired at either 1.5T or 3T, from which we used the T2-weighted (T2W) images for our experiments. Since only a subset of PI-CAI, corresponding to the earlier ProstateX dataset [33], includes expert-annotated labels, while the remainder contains AI-generated prostate zone segmentation masks, we divided PI-CAI into two subsets. The AI-labelled portion (1181 scans), denoted as  $PI\text{CAI}_{train}$ , was used to train and optimise the nnU-Net backbone of MambaX-Net, using 5-fold cross-validation. The expert-labelled subset (195 scans), denoted as  $PI\text{CAI}_{test}$ , was reserved as an external test set to verify that the backbone model achieved performance consistent with SOTA results reported in the literature.

The in-house AS dataset consists of longitudinal scans from 317 patients acquired on a Siemens scanner at either 1.5T or 3T (majority 1.5T), with two time points per patient. Expert labels of WP, PZ and TZ were available for 26 patients (52 scans), selected based on the challenging prostate boundary delineation and low Signal-to-Noise Ratio. While this selection might raise concerns about bias, our intention was to assess the model under difficult conditions; any resulting bias would favour underestimating, rather than inflating performance. Among the 26 patients, 20 (40 scans) were annotated by a board-certified urogenital radiologist and used as a test set ( $AS_{test}$ ), while 6 patients (12 scans) were annotated by a General Practitioner (GP) experienced in prostate MRI and used for MambaX-Net hyperparameter optimisation ( $AS_{val}$ ). The remaining 291 patients (582 scans), denoted as  $AS_{train}$ , were used to train MambaX-Net and had no expert annotations, but were provided with pseudo-labels generated by the pretrained nnU-Net backbone.

### 3.2 Pre-processing

All models shared a common preprocessing pipeline. First, the nnU-Net fingerprinting process [9] was applied to the  $PICAI_{train}$  dataset to determine the normalisation parameters (mean and standard deviation for z-normalisation), voxel spacing, patch size and crop size. Images were resampled to a voxel spacing of  $0.5 \times 0.5 \times 3.0$  mm, cropped to  $384 \times 384$  in the axial plane, and processed as 3D patches of 16 slices. An exception was made for SwinUNETR, which required padding the z-axis to 32 slices to meet its minimum input depth. The resulting configuration was then applied to pre-process  $AS_{train}$ .

### 3.3 Implementation Details

The MambaX-Net experimental pipeline has two stages: First, we pre-trained a standard 3D nnU-Net on  $PICAI_{train}$  (denoted as nnU-Net $PICAI$ ), which serves two key purposes: i) it provides the initial weights for MambaX-Net encoder and decoder and ii) it acts as a pseudo-label generator for self-training, specifically producing pseudo-labels for  $AS_{train}$  at two time points:  $t = 0$  (denoted  $M_0$ ) and  $t = 1$  (denoted  $M_1$ ). Then, using these pseudo-labels, we trained the M-CAM and SEM modules while fine-tuning the MambaX-Net encoder and decoder, which were initialised with nnU-Net $PICAI$  weights. During training,  $M_0$  is provided as input to the model alongside  $I_0$  and  $I_1$ , while  $M_1$  is used exclusively as ground truth for loss calculation, thereby guiding the semi-supervised learning process.

Notably, we did not perform image registration between  $I_0$ ,  $M_0$ , and  $I_1$  before feeding them to the model. The M-CAM using cross-attention is designed to implicitly align features in the latent space, as confirmed by the ablation test results.

To ensure a fair and rigorous comparison, all baseline models followed a similar two-stage training protocol described as follows:

- **nnU-Net, SwinUNETR, and SegMamba:** Each model was first pre-trained on the  $PICAI_{train}$  dataset and fine-tuned on  $AS_{train}$  using pseudo-labels generated by their own respective pre-trained versions ( $model\_name_{PICAI}$ ). Since these are single-time point models, the two longitudinal scans ( $I_0$ ,  $I_1$ ) were treated as independent scans rather than as paired sequential images.
- **DSM:** As a dual-scan model, DSM followed the same training protocol as MambaX-Net. Its encoder and decoder were initialised with nnU-Net $PICAI$  weights, and paired scans ( $I_0$ ,  $I_1$ ) from  $AS_{train}$  were used for fine-tuning the encoder-decoder blocks and training the rest of the modules. Unlike MambaX-Net, DSM does not use  $M_0$  as input and only uses  $M_1$  for loss calculation.

We use the subscripts  $PICAI$  and  $AS$  to denote models trained on the  $PICAI_{train}$  and  $AS_{train}$  datasets, respectively (e.g.,  $model\_name_{PICAI}$  and  $model\_name_{AS}$ ).

All models were trained using the stochastic gradient descent (SGD) optimiser with a batch size of 2 and an early stopping criterion, whereby training was halted if the validation loss (measured to four decimal places) failed to improve over 15 consecutive epochs. Models trained on  $PICAI_{train}$  ( $model\_name_{PICAI}$ ) ran for 1000 epochs with a polynomial decay learning rate scheduler, while models trained on  $AS_{train}$  ( $model\_name_{AS}$ ) were self-trained for 50 epochs using a OneCycle learning rate scheduler. OneCycle was chosen for the  $AS_{train}$  dataset because it promotes super-convergence and improves performance when training data is limited [34]. During training, data augmentation was performed using random intensity shifts, flips, zooms, and the addition of Gaussian noise. Hyperparameter optimisation was performed using Optuna [35] with  $PICAI_{val}$  and  $AS_{val}$  used for  $model\_name_{PICAI}$  and  $model\_name_{AS}$ , respectively. All experiments were implemented using PyTorch 2.7.0, leveraging mixed-precision training for improved efficiency. We used Nvidia V100 (32 GB) and A100 (40 GB) GPUs, depending on the availability of our DGX computing nodes. To enhance the model's robustness and improve prediction accuracy during inference, we apply test-time augmentation (TTA) with random flips and rotations, and average the predictions to get the final result.

## 4 Results

In this section, we present the experimental results evaluating MambaX-Net, with performance measured using DSC and HD95 across the whole prostate (WP), peripheral zone (PZ), and transition zone (TZ). First, we compared MambaX-Net performance against SOTA models on  $AS_{test}$  and analysed the impact of pseudo-labels quality on models' performance. Then we validated the choice of nnU-Net as the optimal backbone for MambaX-Net and evaluated the contribution of individual architectural components by means of an ablation study. All results are reported as the mean  $\pm$  standard deviation of the metrics calculated in 3D, computed across all patients in  $AS_{test}$ . To assess statistical differences ( $\alpha < 0.05$ ), groupwise comparisons were performed using the Friedman rank-sum test followed by Holm's post-hoc analysis.

Table 1: Segmentation performance of MambaX-Net and comparative models on  $AS_{test}$  at time point  $t = 1$ .  $n$  indicates the number of AS patients used for fine-tuning. For each metric, the best results are shown in **bold**. Within each group ( $n$ ), a superscript  $*$  indicates a statistically significant difference ( $\alpha < 0.05$ ) from the best result.

n	Model	DSC $\uparrow$			HD95 (mm) $\downarrow$		
		WP	PZ	TZ	WP	PZ	TZ
0	nnU-Net <sub>PICAI</sub>	$0.45 \pm 0.38^*$	$0.32 \pm 0.36^*$	$0.41 \pm 0.37^*$	$25.1 \pm 16.5^*$	$20.8 \pm 14.5^*$	$25.9 \pm 16.0^*$
	SwinUNETR <sub>PICAI</sub>	<b><math>0.79 \pm 0.14</math></b>	<b><math>0.51 \pm 0.22</math></b>	<b><math>0.77 \pm 0.13</math></b>	<b><math>10.1 \pm 8.0</math></b>	<b><math>11.1 \pm 6.3</math></b>	<b><math>9.4 \pm 7.1</math></b>
	SegMamba <sub>PICAI</sub>	$0.26 \pm 0.18^*$	$0.12 \pm 0.12^*$	$0.27 \pm 0.19^*$	$30.3 \pm 9.7^*$	$30.1 \pm 14.3^*$	$30.0 \pm 8.7^*$
5	nnU-Net <sub>AS</sub>	$0.71 \pm 0.33^*$	$0.57 \pm 0.37^*$	$0.66 \pm 0.35^*$	$16.6 \pm 15.6^*$	$10.4 \pm 9.9^*$	$17.6 \pm 15.4^*$
	SwinUNETR <sub>AS</sub>	$0.82 \pm 0.11^*$	$0.58 \pm 0.18^*$	$0.80 \pm 0.10^*$	$9.2 \pm 7.9^*$	$9.9 \pm 5.6^*$	$9.4 \pm 7.2^*$
	SegMamba <sub>AS</sub>	$0.32 \pm 0.19^*$	$0.17 \pm 0.13^*$	$0.34 \pm 0.20^*$	$29.9 \pm 9.3^*$	$31.4 \pm 18.6^*$	$30.4 \pm 9.6^*$
	DSM	$0.81 \pm 0.14^*$	$0.67 \pm 0.05^*$	$0.75 \pm 0.19^*$	$12.7 \pm 2.9^*$	$7.1 \pm 4.7^*$	$15.0 \pm 13.2^*$
	MambaX-Net	<b><math>0.91 \pm 0.10</math></b>	<b><math>0.85 \pm 0.06</math></b>	<b><math>0.87 \pm 0.14</math></b>	<b><math>8.7 \pm 12.5</math></b>	<b><math>3.6 \pm 1.2</math></b>	<b><math>8.8 \pm 12.7</math></b>
50	nnU-Net <sub>AS</sub>	$0.76 \pm 0.27^*$	$0.64 \pm 0.32^*$	$0.71 \pm 0.29^*$	$14.2 \pm 14.1^*$	$6.2 \pm 5.8^*$	$15.2 \pm 14.3^*$
	SwinUNETR <sub>AS</sub>	$0.83 \pm 0.08^*$	$0.61 \pm 0.15^*$	$0.82 \pm 0.08^*$	$7.8 \pm 5.9^*$	$10.5 \pm 5.5^*$	$8.3 \pm 6.5^*$
	SegMamba <sub>AS</sub>	$0.43 \pm 0.12^*$	$0.28 \pm 0.08^*$	$0.40 \pm 0.13^*$	$27.8 \pm 7.7^*$	$31.1 \pm 10.0^*$	$29.3 \pm 8.0^*$
	DSM	$0.82 \pm 0.13^*$	$0.63 \pm 0.16^*$	$0.77 \pm 0.18^*$	$11.8 \pm 13.5^*$	$6.8 \pm 3.3^*$	$15.1 \pm 14.1^*$
	MambaX-Net	<b><math>0.93 \pm 0.04</math></b>	<b><math>0.85 \pm 0.06</math></b>	<b><math>0.90 \pm 0.07</math></b>	<b><math>7.2 \pm 11.4</math></b>	<b><math>4.8 \pm 6.5</math></b>	<b><math>7.6 \pm 11.3</math></b>
100	nnU-Net <sub>AS</sub>	$0.79 \pm 0.25$	$0.68 \pm 0.32^*$	$0.74 \pm 0.27$	$13.1 \pm 14.0$	<b><math>6.9 \pm 7.1</math></b>	$14.0 \pm 13.9$
	SwinUNETR <sub>AS</sub>	$0.82 \pm 0.10$	$0.59 \pm 0.17^*$	<b><math>0.81 \pm 0.09</math></b>	<b><math>7.9 \pm 5.9</math></b>	$10.9 \pm 5.5^*$	<b><math>8.2 \pm 6.2</math></b>
	SegMamba <sub>AS</sub>	$0.40 \pm 0.14^*$	$0.26 \pm 0.10^*$	$0.38 \pm 0.16^*$	$31.5 \pm 8.0^*$	$28.8 \pm 13.1^*$	$31.9 \pm 7.8^*$
	DSM	$0.78 \pm 0.19$	$0.64 \pm 0.16^*$	$0.72 \pm 0.24^*$	$15.9 \pm 16.0$	$10.5 \pm 11.1$	$16.1 \pm 16.0$
	MambaX-Net	<b><math>0.83 \pm 0.18</math></b>	<b><math>0.82 \pm 0.07</math></b>	$0.77 \pm 0.24$	$15.3 \pm 14.1$	$7.1 \pm 7.9$	$15.6 \pm 14.3$
200	nnU-Net <sub>AS</sub>	$0.78 \pm 0.25$	$0.64 \pm 0.33^*$	$0.73 \pm 0.27$	$16.7 \pm 14.1$	$8.4 \pm 8.6$	$14.5 \pm 13.7$
	SwinUNETR <sub>AS</sub>	<b><math>0.83 \pm 0.09</math></b>	$0.60 \pm 0.16^*$	<b><math>0.82 \pm 0.09</math></b>	<b><math>7.7 \pm 5.7</math></b>	$10.9 \pm 5.6$	<b><math>8.1 \pm 5.9</math></b>
	SegMamba <sub>AS</sub>	$0.41 \pm 0.14^*$	$0.25 \pm 0.13^*$	$0.37 \pm 0.16^*$	$27.9 \pm 10.1^*$	$28.2 \pm 16.3^*$	$28.9 \pm 9.5^*$
	DSM	$0.77 \pm 0.20$	$0.59 \pm 0.23^*$	$0.71 \pm 0.24$	$13.8 \pm 13.8$	$10.1 \pm 8.3$	$14.4 \pm 13.7$
	MambaX-Net	$0.82 \pm 0.18$	<b><math>0.77 \pm 0.10</math></b>	$0.76 \pm 0.23$	$15.1 \pm 14.8$	<b><math>7.9 \pm 8.2</math></b>	$16.2 \pm 15.3$
291	nnU-Net <sub>AS</sub>	<b><math>0.83 \pm 0.20</math></b>	$0.81 \pm 0.10$	$0.78 \pm 0.25$	$12.3 \pm 15.0$	<b><math>5.5 \pm 4.6</math></b>	$13.0 \pm 14.8$
	SwinUNETR <sub>AS</sub>	$0.82 \pm 0.09^*$	$0.58 \pm 0.19^*$	<b><math>0.81 \pm 0.09</math></b>	<b><math>7.8 \pm 4.7</math></b>	$10.6 \pm 5.7^*$	<b><math>7.7 \pm 4.4</math></b>
	SegMamba <sub>AS</sub>	$0.40 \pm 0.13^*$	$0.22 \pm 0.10^*$	$0.40 \pm 0.16^*$	$27.7 \pm 8.6^*$	$23.6 \pm 9.3^*$	$28.3 \pm 8.7^*$
	DSM	$0.77 \pm 0.19^*$	$0.63 \pm 0.16^*$	$0.69 \pm 0.24^*$	$17.1 \pm 15.2^*$	$8.1 \pm 5.7^*$	$18.8 \pm 15.2$
	MambaX-Net	$0.82 \pm 0.20$	<b><math>0.82 \pm 0.07</math></b>	$0.77 \pm 0.25$	$16.4 \pm 15.2$	$6.0 \pm 6.6$	$16.6 \pm 15.4$

### 4.1 MambaX-Net Comparison With SOTA Models

Table 1 summarises the performance of MambaX-Net and the comparative models fine-tuned with different numbers  $n$  of patients from  $AS_{train}$  ( $n = 0, 5, 50, 100, 200$ , and  $291$ ). Here,  $n = 0$  denotes the out-of-the-box performance of models pretrained on  $PICAI_{train}$  without any fine-tuning on  $AS_{train}$ . Results for the dual-scan models (DSM and MambaX-Net) are omitted at  $n = 0$ , since their additional components require training on paired scans from two time points only available in  $AS_{train}$ .

For  $n = 0$ , the three single-scan models showed markedly different levels of robustness to domain shift. The performance of nnU-Net<sub>PICAI</sub> and SegMamba<sub>PICAI</sub> declined significantly, while SwinUNETR<sub>PICAI</sub> was comparatively more stable, showing the smallest performance drop overall; its segmentation of the PZ remained relatively poor. Although fine-tuning on  $AS_{train}$  ( $n > 0$ ) improved the performance of all three single-scan models, none matched their original  $PICAI_{test}$  performance, highlighting the challenge of domain adaptation and motivating strategies like dual-scan architectures.

For  $n \leq 50$ , MambaX-Net consistently outperformed all comparative models, achieving the highest DSC and lowest HD95 scores, especially in the PZ and TZ, with all differences being statistically significant. The next-best models were SwinUNETR<sub>AS</sub> and DSM, which exhibited comparable performance among themselves but markedly lower accuracy than MambaX-Net.

As the number of patients used for fine-tuning grows ( $n \geq 100$ ), the performance gap between most models diminishes for both DSC and HD95, except for SegMamba<sub>AS</sub>, whose performance remains largely unchanged and consistently low across all training sizes. MambaX-Net always achieved either the best or second-best performance in DSC for larger  $n$  values (except for  $n = 291$ ), especially in the PZ, demonstrating consistent competitiveness, albeit without statistically significant improvements. DSM's performance in DSC was only better than SegMamba<sub>AS</sub>, demonstrating that its architectural advantage diminishes compared to SwinUNETR and nnU-Net when training on larger datasets. For HD95, MambaX-Net showed mixed results, ranking second in PZ and being outperformed by both nnU-Net<sub>AS</sub> and SwinUNETR<sub>AS</sub> in the WP and TZ, although these differences are not statistically significant.

To further investigate the variability observed in HD95 across models and training set sizes, we analysed the distribution of HD95 values for each anatomical zone. The boxplots in Figure 3 illustrate these distributions, with MambaX-Net achieving the lowest median and smallest interquartile range. This indicates superior boundary accuracy and higher robustness across patients, particularly notable in the TZ, where other models showed high dispersion. By contrast, SegMamba and nnU-Net exhibited greater variability, reflecting frequent boundary segmentation errors.

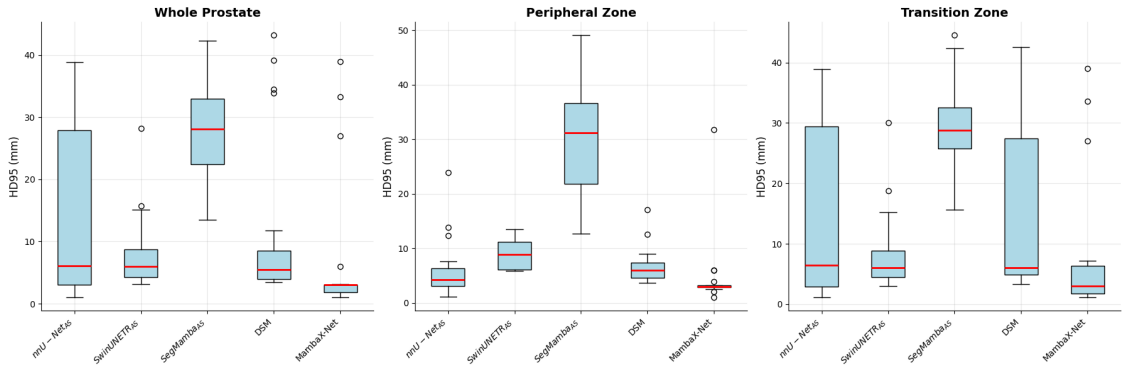


Figure 3: Distribution of HD95 computed on  $AS_{test}$  across WP, PZ, and TZ for the models trained on  $AS_{train}$  with  $n = 50$ .

Figure 4 shows a qualitative comparison of the prostate segmentations for two test patients (Patient 1 and Patient 2) across different models. Patient 1 was selected to showcase moderate-to-good model performance (WP DSC  $> 0.80$ , PZ DSC  $> 0.70$ , TZ DSC  $> 0.75$ ) for all models, except SegMamba, which consistently had poor performance. Patient 2 was selected to showcase a scenario where all models failed to respect anatomical boundaries by segmenting the bladder at the base of the prostate, despite having good DSC scores. Ground-truth segmentations (GT) and model predictions for WP, PZ, and TZ are overlaid on axial T2-weighted images. The models showed distinct error patterns at the prostate's boundaries, and the weakest model, SegMamba<sub>AS</sub>, heavily oversegmented the prostate at the apex. Conversely, SwinUNETR<sub>AS</sub>, nnU-Net<sub>AS</sub>, and DSM typically undersegmented the apex while oversegmenting the base by incorrectly including parts of the bladder as seen in Patient 2. The qualitative results of MambaX-Net on Patient 2, especially at the apex and base of the prostate, suggest that integrating Mamba blocks and the SEM successfully leveraged longitudinal information to refine boundary precision and adapt to the AS domain more effectively than the single-scan models and our previous DSM when trained on limited training data without expert annotations.

A notable finding from these experiments is MambaX-Net's data efficiency. When trained with only  $n = 50$ , MambaX-Net surpasses all other models trained with significantly more data  $n \geq 100$ . This advantage is clear across all quantitative metrics (Table 1) and in qualitative examples (Figure 4), where MambaX-Net produces fewer segmentation errors at the prostate apex and base.

## 4.2 Impact of Pseudo-labels Quality

In this subsection, we assess how pseudo-label quality influences models' accuracy using two experiments. First, we quantified model robustness to label noise by injecting controlled levels of random noise into the pseudo-labels used for training. Second, we evaluated how improving the pseudo-label source affects downstream performance by generating

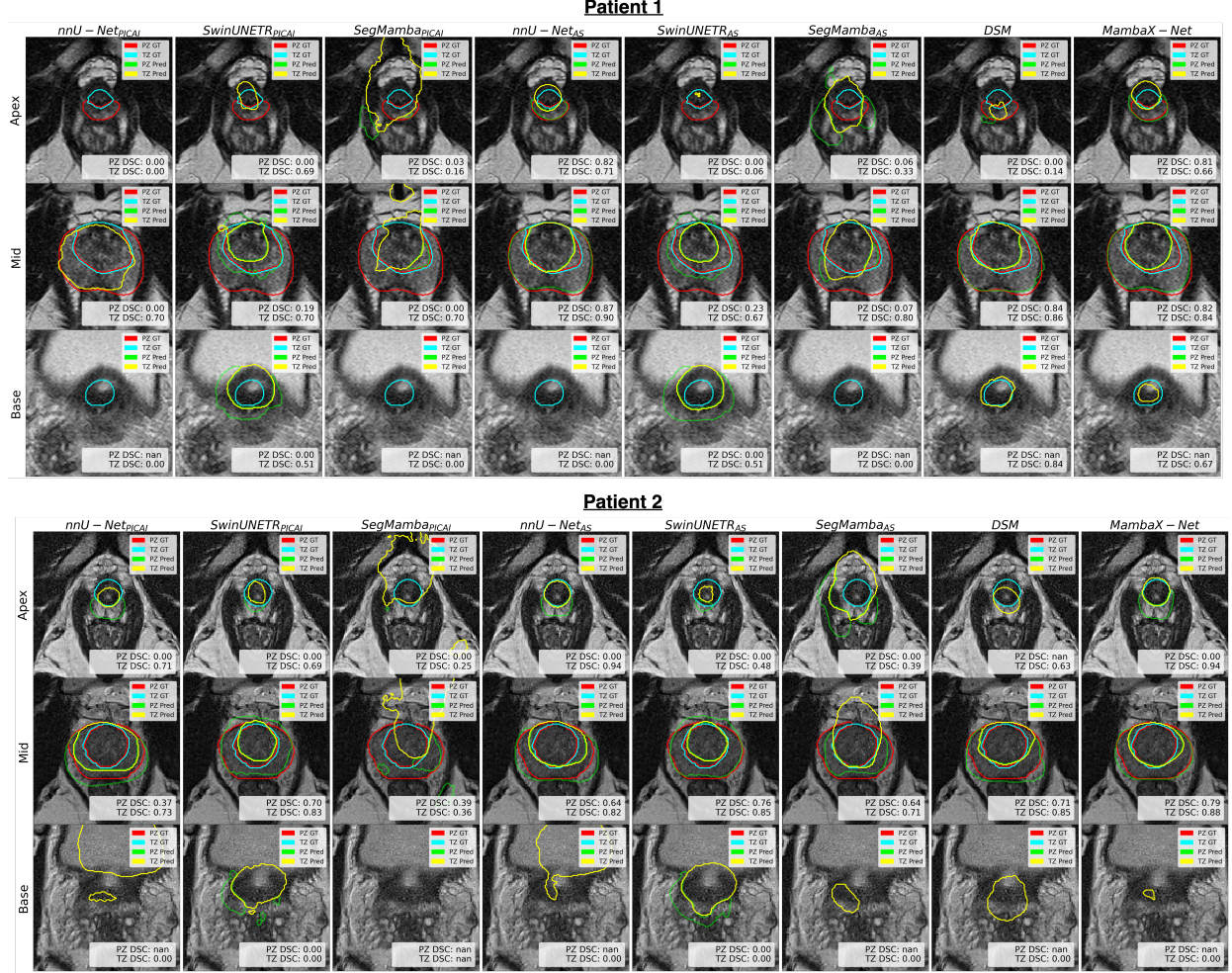


Figure 4: Qualitative comparison of each architecture’s best-performing model on two  $AS_{test}$  patients, comparing models trained with  $n=291$  (nnU-Net<sub>AS</sub>, SwinUNETR<sub>AS</sub> and SegMamba<sub>AS</sub>) against those trained with  $n=50$  (MambaX-Net and DSM).

Table 2: Performance of the models trained on  $AS_{train}$  with pseudo-labels from SwinUNETR<sub>PICAI</sub>, and tested on  $AS_{test}$ . The best model is highlighted in **bold**, with \* indicating a statistically significant difference ( $\alpha < 0.05$ ) from the best model.

Model	DSC $\uparrow$			HD95 (mm) $\downarrow$		
	WP	PZ	TZ	WP	PZ	TZ
nnU-Net <sub>AS</sub>	$0.92 \pm 0.05$	$0.77 \pm 0.12^*$	$0.86 \pm 0.07^*$	$7.2 \pm 8.5$	$9.1 \pm 7.9^*$	<b><math>7.5 \pm 7.9</math></b>
SwinUNETR <sub>AS</sub>	$0.83 \pm 0.08^*$	$0.61 \pm 0.15^*$	$0.82 \pm 0.08^*$	$7.8 \pm 5.9^*$	$10.5 \pm 5.5^*$	$8.3 \pm 6.5^*$
SegMamba <sub>AS</sub>	$0.80 \pm 0.07^*$	$0.58 \pm 0.13^*$	$0.76 \pm 0.09^*$	$18.7 \pm 10.0^*$	$17.1 \pm 8.8^*$	$20.4 \pm 10.9^*$
DSM	$0.84 \pm 0.06^*$	$0.64 \pm 0.08^*$	$0.78 \pm 0.09^*$	$13.3 \pm 11.3^*$	$6.6 \pm 2.5^*$	$15.0 \pm 11.7^*$
<b>MambaX-Net</b>	<b><math>0.94 \pm 0.03</math></b>	<b><math>0.86 \pm 0.06</math></b>	<b><math>0.91 \pm 0.05</math></b>	<b><math>7.1 \pm 11.3</math></b>	<b><math>3.4 \pm 1.2</math></b>	$7.6 \pm 11.2$

new pseudo-labels using the best-performing model at  $n = 0$ , SwinUNETR<sub>PICAI</sub>, and retraining all networks with these higher-quality pseudo-labels.

Given the counter-intuitive finding in Table 1 that MambaX-Net and DSM performance degraded when a larger number of training patients ( $n \geq 100$ ) were used, we investigated in the first experiment whether this behaviour was driven by the accumulation of noise in the pseudo-labels. While a small number act as a form of regularisation, a larger volume would cause overfitting to incorrect supervision and catastrophic forgetting of the model’s valuable pre-trained

knowledge. To examine this effect, we trained the models using 100 patients from  $AS_{train}$ , injecting incremental levels of noise into their pseudo-labels by replacing a percentage of them with Gaussian noise.

Figure 5 compares the mean DSC computed on  $AS_{test}$  across models as the percentage of noise added to the pseudo-labels used for training increases. SegMamba was excluded from this analysis due to its consistently poor performance across all values of  $n$ . As expected, the dual-scan models were more vulnerable to this effect than a single-scan model, as evident from their performance drop at lower levels of injected noise. This is because they process two scans per patient at each training iteration, which could accelerate performance degradation when the labels are noisy. The effect of noisy pseudo-labels mirrored the performance drop seen in Table 1. All models demonstrate robustness to moderate noise levels (up to 60%), with MambaX-Net consistently performing best. However, the dual-scan models suffer a catastrophic performance cliff beyond their respective thresholds of approximately 65% and 75% noise. In contrast, nnU-Net degraded more gradually, even outperforming the dual-scan models above 90% noise. SwinUNETR demonstrated exceptional tolerance to noisy labels, maintaining high performance up to 90% noise. We attribute this robustness to its windowed self-attention mechanism, which mitigates the impact of corrupted boundaries by confining attention to local regions, preventing the propagation of errors.

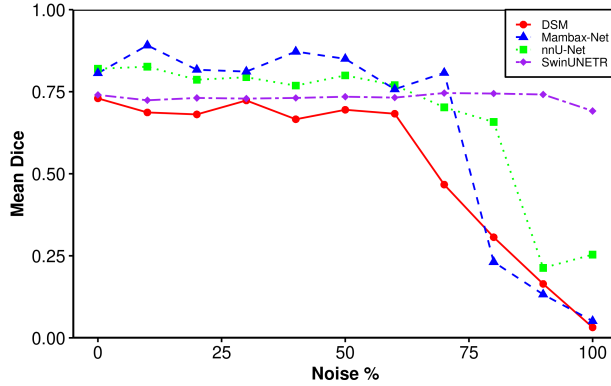


Figure 5: Effect of pseudo-label noise on the model’s performance. Noise % represents the percentage of pseudo-labels replaced with Gaussian noise used for training, the y-axis shows the mean DSC computed on  $AS_{test}$ .

In the experiments presented in subsection 4.1, each model’s performance depended on the quality of its own pseudo-labels, which introduces a potential confounding factor since pseudo-label quality may vary considerably between architectures. To disentangle architectural performance from the influence of pseudo-label quality, we performed an additional controlled experiment where all models were fine-tuned using  $n = 50$  patients from  $AS_{train}$  with high-quality pseudo-labels generated by the SwinUNETR<sub>PICAI</sub> model and evaluated on  $AS_{test}$ .

The results presented in Table 2 confirm MambaX-Net’s architectural effectiveness. It achieved the highest DSC scores across all zones and demonstrated exceptional boundary precision in the clinically crucial peripheral zone (PZ), with an HD95 of 3.4 mm. Statistical analysis confirmed that these results were significantly superior to all baselines for DSC in the PZ and TZ, and for HD95 in the PZ, indicating that MambaX-Net’s performance gain comes directly from its core design. Specifically, its dual-scan approach with Mamba blocks and the SEM provides a more robust method for modelling longitudinal dependencies.

Compared to its  $n = 50$  baseline in Table 1, nnU-Net<sub>AS</sub> showed a significant performance improvement, indicating that nnU-Net outperforms architectures such as SwinUNETR and SegMamba when trained with high-quality pseudo-labels, where inherent noise may act as a regulariser. While SegMamba<sub>AS</sub> improved, it still underperformed compared to nnU-Net<sub>AS</sub>, suggesting it remains sensitive to label noise and may require more training data. In contrast, DSM’s performance remained unchanged from Table 1, indicating that it did not benefit from better pseudo-labels and had already reached a performance plateau.

### 4.3 MambaX-Net Backbone Selection

To identify the best pre-trained backbone for MambaX-Net, we compared three models, namely, nnU-Net<sub>PICAI</sub>, SwinUNETR<sub>PICAI</sub>, and SegMamba<sub>PICAI</sub>, trained on  $PICAI_{train}$  and tested on  $PICAI_{Test}$ . As shown in Table 3, nnU-Net<sub>PICAI</sub> achieved the best performance for both DSC and HD95, consistent with previously reported SOTA results for this benchmark (mean DSC value 0.90, 0.79, and 0.87, for WP, PZ, and TZ, respectively)[20]. Statistical tests confirmed that nnU-Net<sub>PICAI</sub> outperformed both SwinUNETR<sub>PICAI</sub> and SegMamba<sub>PICAI</sub> with statistical significance across all the metrics. Accordingly, nnU-Net<sub>PICAI</sub> was selected as the backbone for MambaX-Net.

Table 3: Segmentation performance of the baseline models on  $PICAI_{Test}$  evaluated using DSC and HD95 across the WP, PZ, and TZ. The best model is highlighted in **bold**, with <sup>\*</sup> indicating a statistically significant difference ( $\alpha < 0.05$ ) from the best value.

Model	DSC $\uparrow$			HD95 (mm) $\downarrow$		
	WP	PZ	TZ	WP	PZ	TZ
nnU-Net <sub>PICAI</sub>	<b><math>0.94 \pm 0.02</math></b>	<b><math>0.85 \pm 0.06</math></b>	<b><math>0.91 \pm 0.04</math></b>	$3.1 \pm 1.5$	$3.3 \pm 2.4$	$3.4 \pm 1.9$
SwinUNETR <sub>PICAI</sub>	$0.92 \pm 0.02^*$	$0.81 \pm 0.06^*$	$0.88 \pm 0.05^*$	$5.5 \pm 2.1^*$	$5.8 \pm 3.1^*$	$6.0 \pm 2.3^*$
SegMamba <sub>PICAI</sub>	$0.91 \pm 0.03^*$	$0.79 \pm 0.07^*$	$0.88 \pm 0.05^*$	$4.0 \pm 1.7^*$	$5.0 \pm 3.4^*$	$4.6 \pm 1.9^*$

#### 4.4 Ablation Study and Model Efficiency Analysis

We performed an ablation study on 6 patients (12 scans) from  $AS_{val}$  to assess the contributions of the SEM and Mamba blocks, and to evaluate whether explicit registration between time points influences model performance. We acknowledge that 6 patients is not a big sample size for ablation studies, but given the difficult and time-consuming nature of manual labelling, most of our limited expert annotations were reserved for testing the models. Results in Table 4 demonstrate that while adding either component individually improves performance, combining them yields the best results, confirming their complementary benefits. Moreover, pre-registering T2W images before inputting them into MambaX-Net provided no measurable performance benefit.

Table 4: Ablation results of MambaX-Net computed on the  $AS_{val}$  data at  $t = 1$  with DSC reported for WP, PZ, and TZ.

T2 Registration	SEM	Mamba	WP	PZ	TZ
$\times$	$\times$	$\times$	0.57	0.46	0.63
$\times$	$\checkmark$	$\times$	0.85	0.75	0.83
$\times$	$\times$	$\checkmark$	0.88	0.75	0.86
$\times$	$\checkmark$	$\checkmark$	0.93	0.85	0.92
$\checkmark$	$\checkmark$	$\checkmark$	0.93	0.84	0.92

Table 5 summarises the model efficiency analysis and highlights a notable trade-off between theoretical complexity and practical performance. Although MambaX-Net is by far the largest model by parameter count (347.6M) and theoretical GFLOPs, its architecture provides significant real-world advantages. It is memory-efficient, requiring substantially less memory (13.8 GB) than the Transformer-based SwinUNETR (25.1 GB), and its inference time (267.8 ms) is highly competitive, outperforming SwinUNETR by approximately 2.4 times and our previous DSM model by 3.5 times, making it a viable option for clinical deployment despite its size.

Table 5: Model efficiency analysis on an Nvidia A100 40 GB GPU.  $Inf\ T$  is the inference time,  $\#Params$  the number of model parameters measured in millions, and  $Mem$  the peak memory in GB used for a single forward and backwards pass.

Model	GFLOPs	#Params	Mem (GB)	Inf T (ms)
nnU-Net	1862.3	44.6	6.6	49.3
SwinUNETR	1888.7	72.6	25.1	649.5
SegMamba	1756.2	66.9	14.2	223.3
DSM	2738.6	44.6	14.3	928.8
MambaX-Net	2883.2	347.6	13.8	267.8

## 5 Conclusion

In this work, we proposed MambaX-Net, a novel dual-scan architecture designed to integrate longitudinal information that leverages pseudo-labels from a pre-trained nnU-Net within a self-training framework. MambaX-Net significantly outperformed SOTA models for prostate MRI segmentation thanks to the newly proposed Mamba-enhanced Cross-Attention Module (M-CAM) and Shape Extractor Module (SEM), which enable the model to integrate longitudinal information and effectively adapt to new domains using only noisy pseudo-labels, demonstrating a feasible path toward clinical translation without manual annotation or explicit image registration. Our experiments showed that, even when trained with a small dataset, MambaX-Net achieved higher performance than nnU-Net or SwinUNETR trained on a larger dataset. Moreover, our investigation revealed that the performance of dual-scan models can degrade more rapidly than that of single-scan models as the volume of noisy pseudo-labels increases. This study has several limitations: (i) validation was performed on a single-institution AS dataset of limited size, used for MambaX-Net development and optimisation. (ii) The quality of the pseudo-labels used for model training was not explicitly accounted for by MambaX-Net during learning. Therefore, future work will focus on validating the framework on larger, multi-centre AS cohorts to confirm its generalisability and on developing more robust self-training strategies, for example, by incorporating uncertainty measures to inform the model about the amount of noise in the labels. Finally, we aim to extend its application to other longitudinal tasks, such as tracking prostate lesion progression in AS patients.

## 6 Acknowledgments

This work was funded by the Engineering & Physical Sciences Research Council (EPSRC), part of the EPSRC DTP, Grant Ref: EP/W524475/1. For the purpose of open access, the author(s) have applied a Creative Commons attribution (CC BY) licence (where permitted by UKRI, 'Open Government Licence' or 'Creative Commons attribution no-derivatives (CC BY-ND) licence' may be stated instead) to any Author Accepted Manuscript version arising.

## References

- [1] Jiajia Chen, Daqing Zhang, Wenyi Yan, Dongrong Yang, and Bairong Shen. Translational Bioinformatics for Diagnostic and Prognostic Prediction of Prostate Cancer in the Next-Generation Sequencing Era. *BioMed Research International*, 2013(1):901578, 2013.
- [2] F.C. Hamdy et al. Fifteen-Year Outcomes after Monitoring, Surgery, or Radiotherapy for Prostate Cancer. *New England Journal of Medicine*, 388(17):1547–1558, 2023.
- [3] Guillaume Ploussard, Olivier Rouvière, Morgan Rouprêt, Roderick van den Bergh, and Raphaële Renard-Penna. The current role of MRI for guiding active surveillance in prostate cancer. *Nature Reviews Urology*, 19(6):357–365, June 2022.
- [4] Alberto Briganti et al. Active Surveillance for Low-risk Prostate Cancer: The European Association of Urology Position in 2018. *European Urology*, 74(3):357–368, 2018.
- [5] Emil Kania, Maciej Janica, Miłosz Nesterowicz, Wojciech Modzelewski, Mateusz Cybulski, and Jacek Janica. Advances and Challenges in Prostate Cancer Diagnosis: A Comprehensive Review. *Cancers*, 17(13):2137, June 2025.
- [6] Ida Arvidsson et al. Artificial intelligence for detection of prostate cancer in biopsies during active surveillance. *BJU International*, 134(6):1001–1009, 2024.
- [7] Xudong Yu, Ruijia Liu, Lianying Song, and et al. Differences in the pathogenetic characteristics of prostate cancer in the transitional and peripheral zones and the possible molecular biological mechanisms. *Frontiers in Oncology*, 13, June 2023.
- [8] Haoxin Zheng et al. AtPCa-Net: anatomical-aware prostate cancer detection network on multi-parametric MRI. *Scientific Reports*, 14(1):5740, March 2024.
- [9] Fabian Isensee, Paul F. Jaeger, Simon A. A. Kohl, Jens Petersen, and Klaus H. Maier-Hein. nnU-Net: a self-configuring method for deep learning-based biomedical image segmentation. *Nature Methods*, 18(2):203–211, February 2021.
- [10] Shravan Bhandary et al. Investigation and benchmarking of U-Nets on prostate segmentation tasks. *Computerized Medical Imaging and Graphics*, 107:102241, July 2023.
- [11] Nuno M. Rodrigues, Sara Silva, Leonardo Vanneschi, and Nickolas Papanikolaou. A Comparative Study of Automated Deep Learning Segmentation Models for Prostate MRI. *Cancers*, 15(5):1467, 2023.

[12] Yufan He, Vishwesh Nath, Dong Yang, Yucheng Tang, Andriy Myronenko, and Daguang Xu. SwinUNETR-V2: Stronger Swin Transformers with Stagewise Convolutions for 3D Medical Image Segmentation. In *Medical Image Computing and Computer Assisted Intervention – MICCAI 2023*, pages 416–426, Cham, 2023. Springer.

[13] Yifei Yan, Rongzong Liu, Haobo Chen, Limin Zhang, and Qi Zhang. CCT-Unet: A U-Shaped Network Based on Convolution Coupled Transformer for Segmentation of Peripheral and Transition Zones in Prostate MRI. *IEEE Journal of Biomedical and Health Informatics*, 27(9):4341–4351, September 2023.

[14] Guantian Huang et al. A Comparative Analysis of U-Net and Vision Transformer Architectures in Semi-Supervised Prostate Zonal Segmentation. *Bioengineering*, 11(9):865, August 2024.

[15] Chetana Krishnan, Ezinwanne Onuoha, Alex Hung, Kyung Hyun Sung, and Harrison Kim. Multi-attention Mechanism for Enhanced Pseudo-3D Prostate Zonal Segmentation. *Journal of Imaging Informatics in Medicine*, February 2025.

[16] Albert Gu and Tri Dao. Mamba: Linear-Time Sequence Modeling with Selective State Spaces, May 2024. arXiv:2312.00752 [cs].

[17] Zhaochu Xing, Tian Ye, Yijun Yang, Guang Liu, and Lei Zhu. SegMamba: Long-Range Sequential Modeling Mamba for 3D Medical Image Segmentation. In *Medical Image Computing and Computer Assisted Intervention – MICCAI 2024*, volume 15008, pages 578–588. Springer, Cham, 2024.

[18] Lijuan Yang, Qiumei Dong, Da Lin, Chunfang Tian, and Xinliang Lü. MUNet: a novel framework for accurate brain tumor segmentation combining UNet and mamba networks. *Frontiers in Computational Neuroscience*, 19:1513059, January 2025.

[19] Rui Zhou, Ju Wang, Guijiang Xia, Jingyang Xing, Hongming Shen, and Xiaoyan Shen. Cascade Residual Multiscale Convolution and Mamba-Structured UNet for Advanced Brain Tumor Image Segmentation. *Entropy*, 26(5):385, April 2024.

[20] Mohammad-Kasim Fassia et al. Deep Learning Prostate MRI Segmentation Accuracy and Robustness: A Systematic Review. *Radiology: Artificial Intelligence*, 6(4):e230138, 2024.

[21] Vincent Andreadczyk et al. Automatic detection and multi-component segmentation of brain metastases in longitudinal MRI. *Scientific Reports*, 14(1):31603, December 2024.

[22] Stefano Cerri et al. An open-source tool for longitudinal whole-brain and white matter lesion segmentation. *NeuroImage: Clinical*, 38:103354, 2023.

[23] Yovin Ransika Yahathugoda, Davide Prezzi, Piyalitt Ittichaiwong, Vicky Goh, Sebastien Ourselin, and Michela Antonelli. Enhanced prostate zone segmentation with multi-timepoint MRI: a cross-attention augmented 3D U-Net approach. In *Medical Imaging 2025: Image Processing*, volume 13406, pages 333–344. SPIE, April 2025.

[24] Lingxiao Yang, Ru-Yuan Zhang, Lida Li, and Xiaohua Xie. SimAM: A Simple, Parameter-Free Attention Module for Convolutional Neural Networks. In *Proceedings of the 38th International Conference on Machine Learning*, volume 139, pages 11863–11874. PMLR, July 2021.

[25] Anton S. Becker et al. Variability of manual segmentation of the prostate in axial T2-weighted MRI: A multi-reader study. *European Journal of Radiology*, 121, December 2019.

[26] Felipe C. Kitamura et al. Lessons Learned in Building Expertly Annotated Multi-Institution Datasets and Hosting the RSNA AI Challenges. *Radiology: Artificial Intelligence*, 6(3):e230227, May 2024.

[27] Jesus Alejandro Alzate-Grisales, Alejandro Mora-Rubio, Francisco García-García, Reinel Tabares-Soto, and María De La Iglesia-Vayá. SAM-UNETR: Clinically Significant Prostate Cancer Segmentation Using Transfer Learning From Large Model. *IEEE Access*, 11:118217–118228, 2023.

[28] Jinyeong Chae and Jihie Kim. An Investigation of Transfer Learning Approaches to Overcome Limited Labeled Data in Medical Image Analysis. *Applied Sciences*, 13(15):8671, 2023.

[29] Hao Guan and Mingxia Liu. Domain Adaptation for Medical Image Analysis: A Survey. *IEEE Transactions on Biomedical Engineering*, 69(3):1173–1185, 2022.

[30] Nitish Mital, Ezgi Özyıldız, and Ali Garjani. Neural Distributed Image Compression with Cross-Attention Feature Alignment. In *2023 IEEE/CVF Winter Conference on Applications of Computer Vision (WACV)*, pages 2497–2506, Waikoloa, HI, USA, 2023. IEEE.

[31] Nabila Abraham and Naimul Mefraz Khan. A Novel Focal Tversky Loss Function With Improved Attention U-Net for Lesion Segmentation. In *2019 IEEE 16th International Symposium on Biomedical Imaging (ISBI 2019)*, pages 683–687, Venice, Italy, 2019. IEEE.

[32] Anindo Saha et al. Artificial intelligence & radiologists at prostate cancer detection in MRI. The PI-CAI Challenge - Grand Challenge.

- [33] Litjens, G., Debats, O., Barentsz, J., N Karssemeijer, and H Huisman. SPIE-AAPM PROSTATEx Challenge Data (Version 2) [dataset], 2017.
- [34] Leslie N. Smith and Nicholay Topin. Super-convergence: very fast training of neural networks using large learning rates. In Tien Pham, editor, *Artificial Intelligence and Machine Learning for Multi-Domain Operations Applications*, page 36, Baltimore, United States, May 2019. SPIE.
- [35] Takuya Akiba, Shotaro Sano, Toshihiko Yanase, Takeru Ohta, and Masanori Koyama. Optuna: A Next-generation Hyperparameter Optimization Framework. In *Proceedings of the 25th ACM SIGKDD International Conference on Knowledge Discovery & Data Mining*, pages 2623–2631, New York, NY, USA, July 2019. Association for Computing Machinery.